RSC Advances

PAPER

View Article Online
View Journal | View Issue

Cite this: *RSC Adv.*, 2017, **7**, 54772

First-principles study of a new structure and oxidation mechanism of Pt_3Zr

Yong Pan,* Shuanglun Wang, Linhu Jia and Xi Zhang

Received 13th October 2017
Accepted 25th November 2017

DOI: 10.1039/c7ra11299h

rsc.li/rsc-advances

Zirconia (ZrO_2)–metal interfaces are interesting for solid oxide fuel cells. Although the oxidation of Pt_3Zr provides a new route for the formation of ZrO_2–Pt interfaces, the crystal structure of Pt_3Zr remains controversial and the oxidation mechanism of Pt_3Zr is unclear. To solve these problems, we use first-principles calculations to explore the crystal structure of Pt_3Zr. We demonstrate a stable structure of Pt_3Zr based on phonon dispersion. Importantly, two new Pt_3Zr structures, Ti_3Pt-type ($Pm\bar{3}m$) and Fe_3Al-type ($Fm\bar{3}m$), are predicted. To study the oxidation mechanism, two possible doped models are considered. The calculated results show that the O atom prefers to occupy the tetrahedral interstitial site (TI) in comparison to the octahedral interstitial site (OI). We find that the oxidizing capacity of the Fe_3Al-type cubic structure is stronger than that of other structures. In particular, we predict that Pt_3Zr exhibits better oxidation capacity in comparison to other metals because of the strong localized hybridization between Zr and O.

1. Introduction

Zirconia (ZrO_2)–metal interfaces have widely used in solid oxide fuel cells (SOFCs), heterogeneous catalysis, gas sensors, *etc.*[1–9] Although ZrO_2 shows excellent chemical and thermal stabilities, the poor electrical conductivity hinders the application because of the requirement of sensitive probing techniques.[10,11] To solve this problem, an effective method is to oxidize Zr on an appropriate metal substrate. However, Zr deposited on a metal substrate should meet three conditions: oxygen reduction reaction (ORR), growth of the oxide layer and better catalytic activity of the metal substrate. In particular, the ORR clearly confirms the degree of oxidation between Zr and the metal substrate. Therefore, high ORR catalytic activity strongly depends on the d-state of the transition metal.[12–14]

Platinum-group-metals are important catalysts because of their excellent chemical and physical properties.[15–18] In particular, Pt is a fascinating catalyst because it effectively promotes the process of ORR.[19–21] Recently, the oxidation behavior of Pt_3Zr (0001) surface was studied by the experiment and first-principles calculations.[22] They found that the weak localized hybridization between Pt and Zr is beneficial to oxidation of Zr metal. Note that the metal addition will accelerate the growth of ZrO_2 film on the Pt_3Zr (0001) surface.[23] Therefore, structural configuration plays a crucial role in ORR and the formation of ZrO_2–Pt interface. Unfortunately, the crystal structure of Pt_3Zr remains controversial. Earlier work suggested that Pt_3Zr is a Au_3Cu-type cubic structure.[24,25] On the contrary, Stalick *et al.* found that Pt_3Zr belongs to a Ni_3Ti-type hexagonal structure,[26] which is different from the previous viewpoint. As a result, the nature of oxidation mechanism of Pt_3Zr is unclear.

To explore the catalytic activity of Pt_3Zr and improve the formation of ZrO_2–Pt interface, in our works, we investigate the crystal structure and oxidation mechanism of Pt_3Zr by using the first-principles calculations. According to the structural feature, we predict two possible cubic structures. Importantly, the structural stability of Pt_3Zr is estimated by the formation enthalpy and phonon dispersion. To examine the oxidation mechanism and oxidation capacity of Pt_3Zr, we calculate and compare the oxygen doped formation energy between O-doped Pt_3Zr and many metals. In particular, we examine the possible adsorption site of Pt_3Zr. Finally, we predict that Pt_3Zr shows better oxidation capacity in comparison to many metals.

2. Model and methods

To explore the oxidation mechanism, we firstly study the crystal structure of Pt_3Zr. To our knowledge, one is that Pt_3Zr is a Ni_3Ti-type hexagonal structure with space group of $P6_3/mmc$. The lattice parameters of hexagonal structure are $a = 5.653$ Å and $c = 9.347$ Å, respectively.[24] Another is that Pt_3Zr belongs to the Au_3Cu-type cubic structure with space group of $Pm\bar{3}m$, and the lattice parameter is $a = 4.051$ Å.[26] In comparison to hexagonal structure, we suggest that Pt_3Zr with cubic structure can promote the oxidation of Pt_3Zr because of the localized hybridization between oxygen and Pt_3Zr. Therefore, we further design two possible structures: Ti_3Pt-type with cubic structure and Fe_3Al-type with cubic structure, respectively. The structural models of Pt_3Zr are shown in Fig. 1.

School of Materials Science and Engineering, Southwest Petroleum University, Chengdu 610500, China. E-mail: panyong10@mails.jlu.edu.cn; Fax: +86-028-83037406; Tel: +86-028-83037401

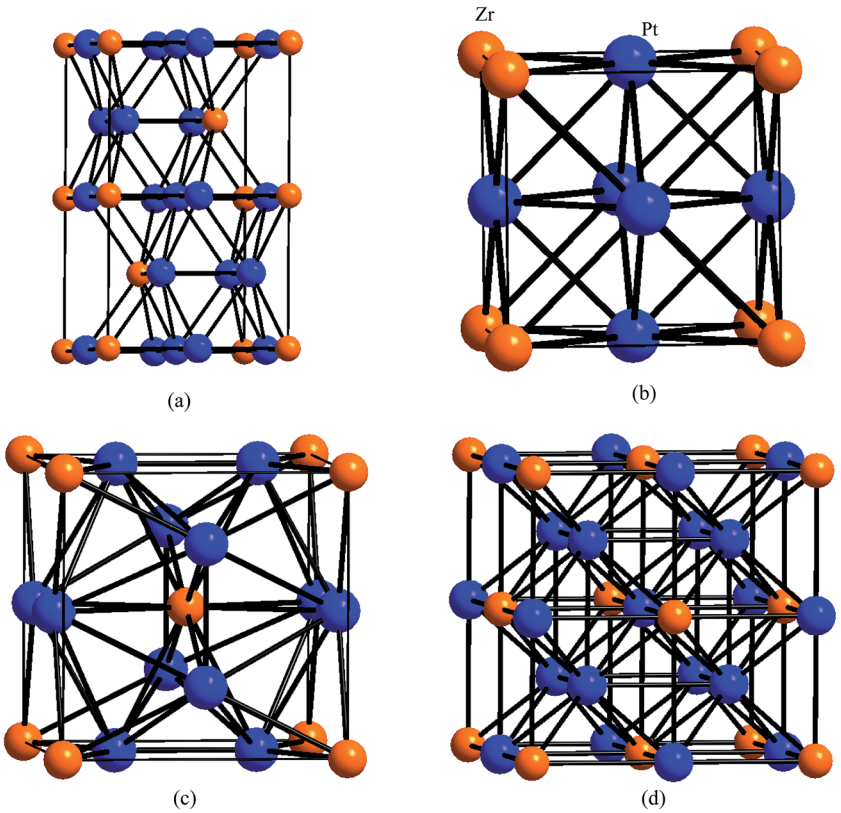

Fig. 1 Structural model of Pt_3Zr, (a) Ni_3Ti-type with hexagonal structure, (b) Au_3Cu-type with cubic structure, (c) Ti_3Pt-type with cubic structure and (d) Fe_3Al-type with cubic structure, respectively.

In this paper, the total energy, structural information, electronic structure and chemical bonding of Pt_3Zr and O-doped Pt_3Zr were calculated by using the first-principles calculations, as implemented in the CASTEP code.[27] The exchange–correlation-functional was calculated by using the generalized gradient approximation (GGA) within PW91 functional.[28,29] To treat the interaction between electrons and the ions, the atomic configurations of O, Pt and Zr were $2s^2 2p^4$, $5p^6 5d^9 6s^1$ and $4p^6 4d^2 5s^2$, respectively. Based on the convergence test, the plane-wave basis set for electron wave function with cutoff energy of 400 eV was used. The *k*-point grids of $10 \times 10 \times 5$ for Ni_3Ti-type structure, $12 \times 12 \times 12$ for Au_3Cu-type structure, $10 \times 10 \times 10$ for Ti_3Pt-type structure, $11 \times 11 \times 11$ for Fe_3Al-type structure, $14 \times 14 \times 8$ for Zr and $17 \times 17 \times 17$ for Pt were treated, respectively. To examine the dynamically stable, the phonon calculation was carried out by using the supercell method within the PHONON code.[30]

3. Results and discussions

3.1 Structural prediction

The structural stability of Pt_3Zr is measured by the formation enthalpy and phonon dispersion, respectively. The equation of formation enthalpy (ΔH) is given by:

$$\Delta H = E_{Pt_3Zr} - 3E_{Pt} - E_{Zr} \quad (1)$$

where E_{Pt_3Zr}, E_{Pt} and E_{Zr} are the total energy of Pt_3Zr, isolated Pt atom and isolated Zr atom, respectively.

Table 1 lists the calculated lattice parameters, density, and formation enthalpy of Pt_3Zr with four structures. It can be seen that these structures are thermodynamically stable at the ground state because the calculated formation enthalpy of these structures is smaller than zero. Our predicted two structures (Ti_3Pt-type and Fe_3Al-type) are also thermodynamically stable. Importantly, the calculated formation enthalpy of Ni_3Ti-type structure is −8.188 eV per atom, which is smaller than that of Au_3Cu-type structure. The slight difference implies that external condition is easy to result in phase transition from Ni_3Ti-type structure to Au_3Cu-type structure. This result is similar to the Fairbank's viewpoint.[24]

Table 1 Calculated equilibrium lattice parameters, *a*-axis and *c*-axis (Å), density, ρ (g cm^{-3}) and formation enthalpy, ΔH (eV per atom) of Pt_3Zr

Structure	Method	*a*	*c*	ρ	ΔH
Ni_3Ti-type	GGA	5.742	9.398	16.75	−8.188
	Exp[24]	5.653	9.347		
Au_3Cu-type	GGA	4.061		17.77	−8.178
	Theo[25]	3.980			
	Exp[26]	4.051			
Ti_3Pt-type	GGA	5.198		16.00	−7.918
Fe_3Al-type	GGA	6.513		16.26	−7.871

In addition to thermodynamically stable, the dynamically stable of Pt_3Zr should examine follow. To study the dynamically stable, Fig. 2 displays the calculated phonon dispersion curves of Pt_3Zr with four structures. It is clear that Pt_3Zr with Ni_3Ti-type structure is a dynamically unstable because the imaginary phonon frequency is observed in this structure. However, we find that there is no imaginary phonon frequency in Au_3Cu-type structure, indicating that this structure is a dynamically stable at the ground state. Based on the first-principles calculations, we demonstrate the Stalick's viewpoint. Importantly, we predict two new Pt_3Zr structures (Ti_3Pt-type and Fe_3Al-type) because no imaginary phonon frequencies are found in these structures.

To further insight into the nature of dynamically stable, Fig. 3 shows the calculated phonon density of state (PhDOS) of Pt_3Zr with four structures. It can be seen that negative frequencies are found in Ni_3Ti-type structure, indicating that this structure is a mechanically unstable at the ground state. The calculated PhDOS profile reveals that the mechanically unstable of Ni_3Ti-type is attributed to the vibration of Pt atom at low frequency region. However, Au_3Cu-type, Ti_3Pt-type and Fe_3Al-type structures are mechanically stable because no negative frequencies are observed in these structures. In particular, the whole low frequency model of Au_3Cu-type structure derives from the vibration of Pt atom and Zr atom. With increasing frequency, Zr's vibration plays an important role in thermodynamic properties. Therefore, it is concluded that the structural stability of Pt_3Zr is markedly influenced by Pt–Zr bond.

To further reveal the structural stability, the structural information of Pt_3Zr is discussed. As listed in Table 1, the calculated lattice parameters of Ni_3Ti-type structure (space group: $P6_3/mmc$, no: 194) are $a = 5.742$ Å and $c = 9.398$ Å, which are in good agreement with the experimental data.[24] In this structure (see Fig. 1(a)), the alternative Pt layer and Pt–Zr layer can be viewed along the c-axis. In particular, each Zr atom is surrounded by 4 Pt atoms at Pt–Zr layer. Therefore, Pt–Zr bond (2.601 Å) can improve the structural stability of Pt_3Zr with Ni_3Ti-type structure. However, the cohesive force between layers is determined by the bond strength of Pt–Pt bond and part of Pt–Zr bond. In other words, Pt–Pt and Pt–Zr bonds play a key role in structural stability. The calculated bond length of Pt–Pt and Pt–Zr bonds is 2.924 Å and 2.968 Å, respectively.

For Au_3Cu-type structure (see Fig. 1(b)), the calculated lattice parameter is $a = 4.061$ Å, which is in excellent agreement with the experimental data and theoretical results.[25,26] Note that the symmetrical Pt–Zr bonds effectively improve it's structural stability. The calculated bond length of Pt–Zr bond is 2.871 Å, which is similar to the previous theoretical result.[31] Note that the bond length of Pt–Zr bond of Au_3Cu-type structure is slightly smaller than the corresponding bond for Ni_3Ti-type structure, indicating that the structural feature of the former can obviously improve the structural stability in comparison to the latter. Thus, we should consider the cubic structure to oxidize Zr.

The calculated lattice parameter of Ti_3Pt-type and Fe_3Al-type structures is $a = 5.198$ Å and $a = 6.513$ Å, respectively. From Fig. 1, Ti_3Pt-type structure is similar to Nb_3Si-type structure. In comparison to Au_3Cu-type structure, Pt atom in Ti_3Pt-type structure occurs migration from (0.50, 0, 0.50) site to (0.25, 0, 0.50) site. As a result, the variation of atomic position changes the localized hybridization between Pt and Zr, which forms two different Pt–Zr bonds. The calculated bond length of Pt–Zr bond is 2.599 Å and 2.906 Å, respectively. In particular, the atomic configuration can provide a large number of interstitial sites to adsorb oxygen. In addition, we find that the calculated lattice parameter of Ti_3Pt-type and Fe_3Al-type structures is larger than that of Au_3Cu-type structure.

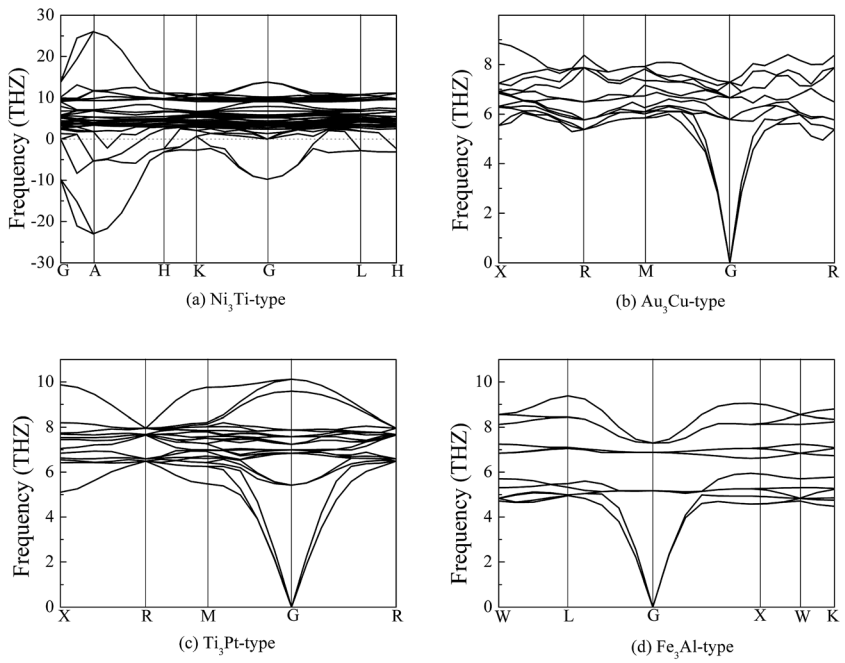

Fig. 2 Calculated phonon dispersion curves of Pt_3Zr, (a) Ni_3Ti-type structure, (b) Au_3Cu-type structure, (c) Ti_3Pt-type structure and (d) Fe_3Al-type structure, respectively.

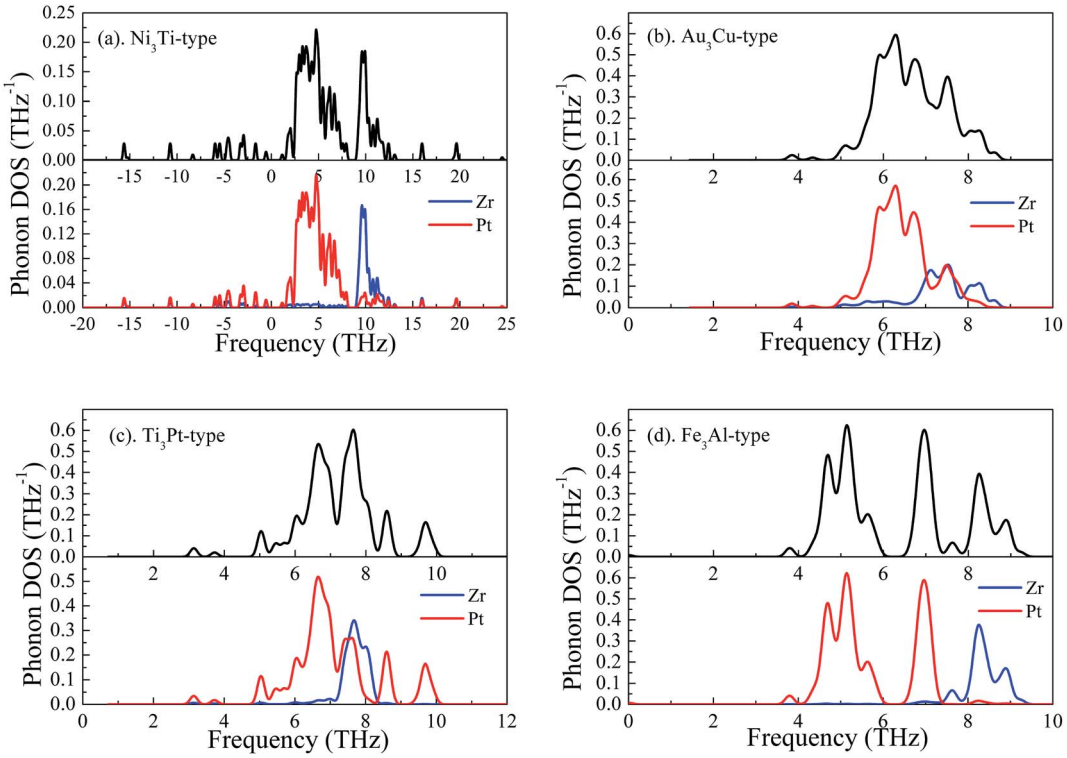

Fig. 3 Phonon density of state of Pt_3Zr, (a) Ni_3Ti-type structure, (b) Au_3Cu-type structure, (c) Ti_3Pt-type structure and (d) Fe_3Al-type structure, respectively.

For Fe_3Al-type structure, Pt atom migrates from (0.50, 0, 0.50) site to (0.25, 0.25, 0.25) site. Each Pt atom is surrounded by 4 Zr atoms and 8 Pt atoms. The calculated bond length of Pt–Zr bond is 2.820 Å. Importantly, the network Pt–Zr bonds can improve the structural stability of Pt_3Zr.

To reveal the nature of chemical bonding, Fig. 4 shows the calculated density of state (DOS) of Pt_3Zr with four structures. We can see that the DOS profile of Pt_3Zr is composed of Pt-5d state and Zr-4d state. The strong localized hybridization between Pt and Zr forms the Pt–Zr bond. It is worth noticing

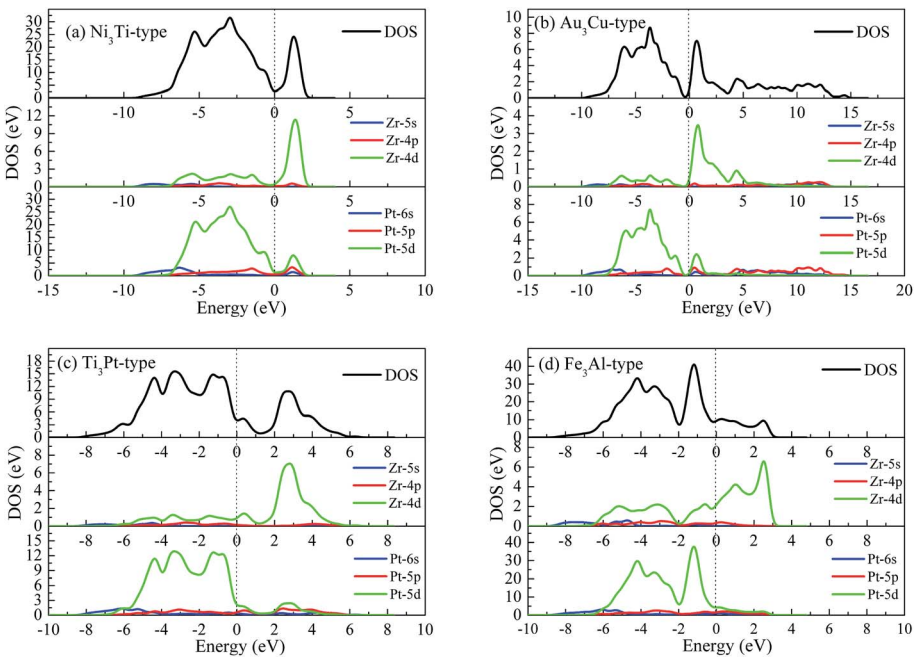

Fig. 4 Total and partial density of state (DOS) of Pt_3Zr, (a) Ni_3Ti-type structure, (b) Au_3Cu-type structure, (c) Ti_3Pt-type structure and (d) Fe_3Al-type structure, respectively.

that the DOS profile of Ni_3Ti-type structure is similar to Au_3Cu-type structure. From Fig. 4, there is a deep valley near Fermi level (E_F), which separates the bonding state and antibonding state. For Ti_3Pt-type and Fe_3Al-type structures, however, the Zr-PDOS profile right shifts from E_F to high energy region. That is to say, Pt's migration weakens the localized hybridization between Pt and Zr. As a result, Pt–Pt bond plays an important role in structural stability, particularly for catalytic properties.

3.2 Oxidation mechanism

We suggest that the formation of ZrO_2–Pt interface strongly depends on the interaction between Pt_3Zr and O atom. To examine the formation of ZrO_2–Pt interface, we calculate the oxygen doped formation energy of O-doped Pt_3Zr. In particular, we discuss and analyze the chemical bonding of O-doped Pt_3Zr to reveal the formation of ZrO_2–Pt interface. It must be mentioned that the formation of ZrO_2 film is related to the interstice radius of Pt_3Zr, which is determined by the atomic configuration of Pt_3Zr. Therefore, it is necessary to insight into the oxidation mechanism of Pt_3Zr.

According to the first-principles calculations, we consider the oxidation behavior of three stable Pt_3Zr structures: Au_3Cu-type, Ti_3Pt-type and Fe_3Al-type, respectively. To reveal the oxidation mechanism, we design the possible interstice models: tetrahedral interstice site (TI) and octahedral interstice site (OI), respectively. Oxygen mechanism of Pt_3Zr is measured by the oxygen doped formation energy (E_{ad}), which is given by:

$$E_{ad} = E^{O}_{Pt_3Zr} - E_{Pt_3Zr} - \mu_O \quad (2)$$

where $E^{O}_{Pt_3Zr}$ and E_{Pt_3Zr} are the total energy of O-doped Pt_3Zr and parent Pt_3Zr at the ground state, respectively. μ_O is the chemical potential of O atom. Generally, the negative oxygen doped formation energy indicates the thermodynamically stable at the ground state.

To explore the catalytic activity of Pt_3Zr, we calculate and compare the capacity of oxygen between Pt_3Zr and many metals. Firstly, we explore the oxidation mechanism of Pt_3Zr. From Fig. 1, Au_3Cu-type is a typical cubic structure. Therefore, we design two possible occupied sites: TI site and OI site, respectively. However, the structural feature of Ti_3Pt-type structure is more complex than that of Au_3Cu-type structure. According to the structural feature, we design two different OI sites and one TI site. Although the doped model of Fe_3Al-type structure is similar to Au_3Cu-type structure, the atomic interaction of the former is stronger than the latter. That is to say, Fe_3Al-type structure is easily to adsorb a large number of oxygen.

Fig. 5 shows the calculated oxygen doped formation energy of O-doped Pt_3Zr and many metals. We can conclude that TI model is more thermodynamically stable than that of OI model because the calculated oxygen doped formation energy of the former is lower than the latter. This discrepancy is attributed to the localized hybridization between O and Zr. For Pt_3Zr, TI site can effectively improve the charge interaction between Zr and O, which forms the Zr–O bond. In particular, O atom prefers to occupy the TI site of Fe_3Al-type structure in comparison to other structures. Therefore, we can adjust the crystal structure of

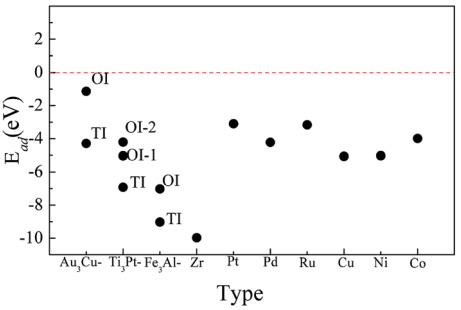

Fig. 5 Calculated oxygen adsorption energy of O-doped Pt_3Zr at tetrahedral interstice site (TI) and octahedral interstice site (OI), together with many metals.

Pt_3Zr to promote the formation of ZrO_2. In particular, the calculated oxygen doped formation energy of Fe_3Al-type with TI site is about −9.029 eV, which is smaller than that of other structures. This result indicates that Pt_3Zr with Fe_3Al-type structure shows the better catalytic activity in comparison to other structures. This reason is attributed to the atomic configuration of Pt_3Zr.

As we know, many metals such as Pt, Cu, Ni and Co *etc.* are important parts of solid oxide fuel cells.[32–35] To estimate the catalytic activity of Pt_3Zr, we compare the oxygen doped formation energy between Pt_3Zr and many metals. As shown in Fig. 5, the calculated oxygen doped formation energy of metal Zr is −10.068 eV, which is smaller than that of Pt_3Zr. This result indicates that metal Zr shows better oxidation capacity in comparison to Pt_3Zr. This is why ZrO_2 has been widely investigated over the last years. Importantly, although the oxygen doped formation energy of Pt_3Zr is larger than that of metal Zr, the oxygen doped formation energy of Pt_3Zr is smaller than that of other metals (see Fig. 5). The calculated electronic structure shows that the better oxidation capacity of Pt_3Zr derives from the strong localized hybridization between O and metal Zr. As mentioned above, we can predict that Pt_3Zr is expected to have better catalytic activity in comparison to other metals.

To reveal the nature of the oxidation mechanism, we further analyze the chemical bonding of O-doped Pt_3Zr. The first-principle calculations show that the bond length of Zr–O bond for Au_3Cu-type structure and Ti_3Pt-type structure is 2.026 Å and 2.014 Å, respectively, which are smaller than the corresponding Zr–O bond (2.05 Å) of ZrO_2.[36,37] However, the calculated bond length of Zr–O bond of Fe_3Al-type structure is 2.076 Å, which is close to the bond length of Zr–O bond for ZrO_2. On the other hand, the calculated electronic localization density shows that there is a strong localized hybridization between Pt and O for Au_3Cu-type structure. The calculated bond length of Pt–O bond is 2.117 Å. However, Pt–O antibonding state in Ti_3Pt-type and Fe_3Al-type structures is found. In other words, Ti_3Pt-type and Fe_3Al-type structures are beneficial to the formation of ZrO_2. The oxidation mechanism of Pt_3Zr with three structures is shown in Fig. 6. As mentioned above, we predict that Pt_3Zr with Fe_3Al-type structure is beneficial to the formation of ZrO_2.

To gain insight the nature of oxidation behavior, Fig. 7 shows the calculated DOS of O-doped Pt_3Zr with three structures. We

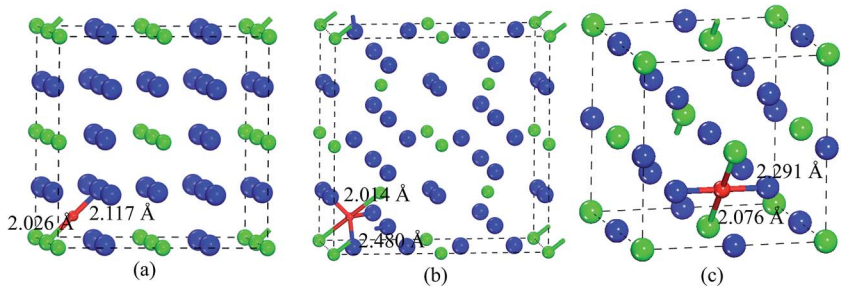

Fig. 6 Oxygen adsorption mechanism of Pt_3Zr, (a) Au_3Cu-type structure, (b) Ti_3Pt-type structure and (c) Fe_3Al-type structure, respectively.

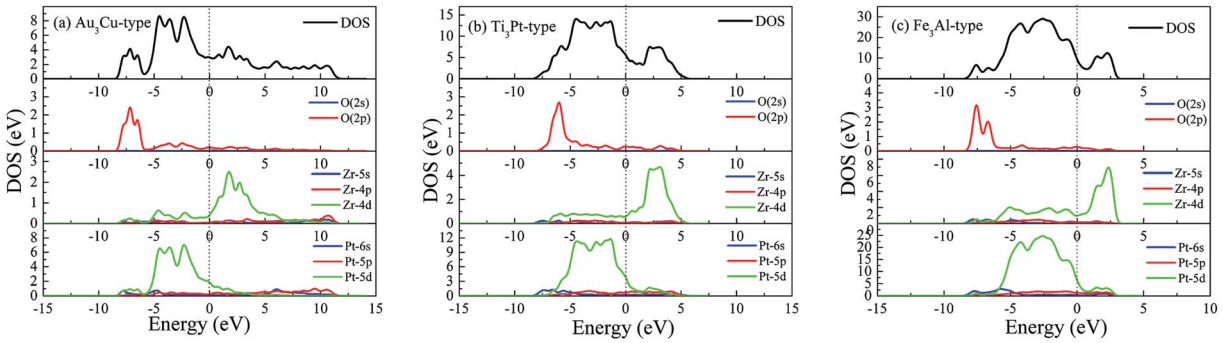

Fig. 7 Total and partial density of state (DOS) of O-doped Pt_3Zr, (a) Au_3Cu-type structure, (b) Ti_3Pt-type structure and (c) Fe_3Al-type structure, respectively.

observe that the DOS profile of Pt_3Zr is mainly contributed by Pt-5d state and Zr-4d state. The strong localized hybridization between Pt and Zr forms the Pt–Zr bond. However, oxygen addition can improve the charge equilibrium between Pt and Zr. As shown in Fig. 7, we can see that the charge interaction between O and Zr forms the Zr–O bond, which demonstrates the existence of Zr–O bond.

4. Conclusions

In summary, we apply first-principles calculations to study the crystal structure and oxidation mechanism of Pt_3Zr. To explore the stable structure, we calculate the formation enthalpy, phonon dispersion, lattice parameters and electronic structure of Pt_3Zr. In addition, we predict two possible new Pt_3Zr structures: Ti_3Pt-type (space group: $Pm\bar{3}m$, no. 223) and Fe_3Al-type (space group: $Fm\bar{3}m$, no. 225). To investigate the oxidation mechanism, we calculate the oxygen doped formation energy and chemical bonding of O-doped Pt_3Zr. In particular, we compare the oxygen doped formation energy of Pt_3Zr and many metals.

The calculated results show that although Pt_3Zr with hexagonal structure is more thermodynamically stable than that of cubic structure, hexagonal structure is a dynamically unstable at the ground state. The calculated oxygen doped formation energy of TI site is smaller than that of OI site. The calculated oxygen doped formation energy of Pt_3Zr with Fe_3Al-type structure is smaller than that of other structures. The calculated chemical bonding shows that Pt_3Zr with Fe_3Al-type structure is easy to form the ZrO_2 because of the formation of Zr–O bond. In particular, the calculated oxygen doped formation energy of Fe_3Al-type with TI site is smaller than that of other metals, indicating that Pt_3Zr shows the good catalytic activity in comparison to metals.

Conflicts of interest

There are no conflicts to declare.

Acknowledgements

This work is supported by grants from the Sichuan Provincial Colleges' Sate Key Laboratory of Oil and Gas Reservoir Project (X151517KCL36) and the national natural science foundation of China (No. 51267007). We acknowledge the help from Lady Yun Zheng.

References

1 H. Y. T. Chen, S. Tosoni and G. Pacchioni, *ACS Catal.*, 2015, **5**, 5486–5495.
2 L. M. Toscani, A. Raievich, M. C. Aantini, D. G. Lamas and S. A. Larrondo, *J. Phys. Chem. C*, 2016, **120**, 24165–24175.
3 A. P. Kulkarni, S. Giddey and S. P. S. Badwal, *J. Phys. Chem. C*, 2016, **120**, 15675–15683.
4 N. S. Yuzbasi, A. M. Kierzkowska, Q. Imtiaz, P. M. Abdala, A. Kurlov, J. L. M. Rupp and C. R. Muller, *J. Phys. Chem. C*, 2016, **120**, 18977–18985.

5 P. Li, X. Chen, X. Wang, J. Shao, G. Lin, H. Yang, Q. Yang and H. Chen, *Energy Fuels*, 2017, **31**, 3979–3986.
6 A. Ganesan, M. Narayanasamy, K. Shunmugavel and I. J. Chinnappa, *Int. J. Hydrogen Energy*, 2016, **41**, 8963–8977.
7 F. Menegazzo, M. Signoretto, D. Marchese, F. Pinna and M. Manzoli, *J. Catal.*, 2015, **326**, 1–8.
8 E. Ciftyurek, C. D. Mcmillen, K. Sabolsky and E. M. Sabolsky, *Sens. Actuators, B*, 2015, **207**, 206–215.
9 J. Ftouni, A. M. Murillo, A. Goryachev, J. P. Hofmann, E. J. M. Hensen, L. Lu, C. J. Kiely, P. C. A. Bruijnincx and B. M. Weckhuysen, *ACS Catal.*, 2016, **6**, 5462–5472.
10 F. Giannici, G. Canu, M. Gambino, A. Longo, M. Salome, M. Viviani and A. Martorana, *Chem. Mater.*, 2015, **27**, 2763–2766.
11 M. Kuzminska, T. V. Kovalchuk, R. Backov and R. M. Gaigneaux, *J. Catal.*, 2014, **320**, 1–8.
12 S. Grieshammer, *J. Phys. Chem. C*, 2017, **121**, 15078–15084.
13 H. H. Li, S. Y. Ma, Q. Q. Fu, X. J. Liu, L. Wu and S. H. Yu, *J. Am. Ceram. Soc.*, 2015, **137**, 7862–7868.
14 Y. Sha, T. H. Yu, B. V. Merinov and W. A. Goddard, *ACS Catal.*, 2014, **4**, 1189–1197.
15 L. A. Avakyan, N. A. Kolpacheva, E. V. Paramonova, J. Singh, U. Hartfelder, J. A. V. Bokhoven and L. A. Bugaev, *J. Phys. Chem. C*, 2016, **120**, 28057–28066.
16 H. Ostrom, H. Oberg, H. Xin, J. Larue, M. Beye, M. D. Angela and A. Nilsson, *Science*, 2015, **347**, 978–982.
17 K. Ding, A. Gulec, A. M. Johnson, N. M. Schweitzer, G. D. Stucky, L. D. Marks and P. C. Stair, *Science*, 2015, **350**, 189–192.
18 Y. Pan, C. Jin and P. Mao, *J. Electron. Mater.*, 2017, **46**, 6639–6645.
19 H. Sohn and U. Ozkan, *Energy Fuels*, 2016, **30**, 5309–5322.
20 J. Durst, M. L. Haro, L. Dubau, M. Chatenet, Y. S. Olivier, L. Guetaz, P. B. Guillemaud and F. Maillard, *J. Phys. Chem. Lett.*, 2014, **5**, 434–439.
21 C. Zhang, S. Y. Hwang, A. Trout and Z. Peng, *J. Am. Chem. Soc.*, 2014, **136**, 7805–7808.
22 M. Antlanger, W. M. Schmölzer, J. Pavelec, F. Mittendorfer and J. Redinger, *Phys. Rev. B: Condens. Matter Mater. Phys.*, 2012, **86**, 035451.
23 J. J. Choi, W. M. Schmolzer, I. Valenti, P. Luches, F. Mittendorfer, J. Redinger, U. Diebold and M. Schmid, *J. Phys. Chem. C*, 2016, **120**, 9920–9932.
24 G. B. Fairbank, C. J. Humphreys, A. Kelly and C. N. Jones, *Intermetallics*, 2000, **8**, 1091–1100.
25 Y. Pan, Y. Lin, X. Wang, S. Chen, L. Wang, C. Tong and Z. Cao, *J. Alloys Compd.*, 2015, **643**, 49–55.
26 J. K. Stalick and R. M. Waterstrat, *J. Alloys Compd.*, 2007, **430**, 123–131.
27 M. D. Segall, P. J. D. Lindan, M. J. Probert, C. J. Pickard, P. J. Hasnip, S. J. Clark and M. C. Payne, *J. Phys.: Condens. Matter*, 2002, **14**, 2717–2744.
28 J. P. Perdew and Y. Wang, *Phys. Rev. B: Condens. Matter Mater. Phys.*, 1992, **45**, 13244–13249.
29 G. Kresse and D. Joubert, *Phys. Rev. B: Condens. Matter Mater. Phys.*, 1999, **59**, 1758–1775.
30 S. Baroni, S. d. Gironcoli, A. D. Corso and P. Giannozzi, *Rev. Mod. Phys.*, 2001, **73**, 515.
31 Y. Pan, W. Guan, M. Wen, J. Zhang, C. Wang and Z. Tan, *J. Alloys Compd.*, 2014, **585**, 549–554.
32 Z. Zheng, C. Sun, R. Dai, S. Wang, X. Wu, X. An, Z. Wu and C. Xie, *Energy Fuels*, 2017, **31**, 3091–3100.
33 M. Deutsch, F. Horvath, C. Knoll, D. Lager, C. G. Mayer, P. Weinberger and F. Winter, *Energy Fuels*, 2017, **31**, 2324–2334.
34 K. Nakao, T. Ishimoto and M. Koyama, *J. Phys. Chem. C*, 2016, **120**, 16641–16648.
35 X. Yang, Y. Wang, M. Li, B. Sun, Y. Li and Y. Wang, *Energy Fuels*, 2016, **30**, 2198–2203.
36 W. Piskorz, J. Grybos, F. Zasada, S. Cristol, J. F. Paul, A. Adamski and Z. Sojka, *J. Phys. Chem. C*, 2011, **115**, 24274–24286.
37 M. Taddei, F. Costantino, V. Manuali and R. Vivani, *Inorg. Chem.*, 2011, **50**, 10835–10843.

